IOP Publishing Superconductor Science and Technology
Supercond. Sci. Technol. **28** (2015) 024003 (15pp) doi:10.1088/0953-2048/28/2/024003

Modelling current voltage characteristics of practical superconductors

A Badía-Majós[1] **and C López**[2]

[1] Departamento de Física de la Materia Condensada-I.C.M.A., Universidad de Zaragoza-C.S.I.C., María de Luna 1, E-50018 Zaragoza, Spain
[2] Departamento de Física y Matemáticas, Universidad de Alcalá de Henares, E-28871 Alcalá de Henares, Spain

E-mail: anabadia@unizar.es and carlos.lopez@uah.es

Received 19 June 2014, revised 5 October 2014
Accepted for publication 17 October 2014
Published 24 December 2014

Abstract

Based on recent experimental results, and in the light of fundamental physical properties of the magnetic flux in type-II superconductors, we introduce a practical expression for the material law to be applied in numerical modelling of superconducting applications. Focusing on the computational side, in this paper, previous theory is worked out, so as to take the celebrated form of a *power-law-like* dependence for the current voltage characteristic. However, contrary to the common approach in numerical studies, this proposal suits the general situation of current density flow with components either parallel or perpendicular to the local magnetic field, and different constraints applying on each component. Mathematically, the theory is generated from an elliptic locus defined in terms of the current density vector components. From the physical side, this contour establishes the boundary for the onset of entropy production related to overcritical current flow in different conditions. The electric field is obtained by partial differentiation and points perpendicular to the ellipse. Some numerical examples, inspired by the geometry of a two-layer helical counter-wound cable are provided. Corrections to the widespread use of the implicit isotropic assumption (physical properties only depend on the modulus of the current density vector) are discussed, and essentially indicate that the current carrying capacity of practical systems may be underestimated by using such simplification.

Keywords: modelling HTS, critical currents, current voltage

(Some figures may appear in colour only in the online journal)

1. Introduction

Significant progress in the synthesis of superconducting materials has recently led to the demand for modelling tools that allow the precise simulation of their physical behavior in potential applications. Thus, a rapid emergence of simulation studies in electrical machines, solenoids and complex cable geometries has occurred. However, several issues have been identified related to the implementation of computational codes at the engineering level, among which a fundamental question remains: Are developers using a sound material law? More specifically, when a conducting sample is subject to a certain process, a standard practice in computational electromagnetism is to describe its behavior through the so-called current–voltage characteristic ($\{V,\ I\}$ relation) at the macroscopic level. The concern is whether the formulas used for superconductors, that somehow mimic their counterpart for conventional conductors rely on a solid ground, and to what extent they can be used in different configurations.

To start with, a basic consensus has been reached that a functional *power-law* dependence, i.e.: V is negligibly small for transport current values below a certain threshold value (I_c) and quickly increases above, i.e. $V \propto (I/I_c)^N$, typically with $N \gg 1$, encodes reasonably the observed behavior of type-II superconductors in the range of applications. More in detail, being concerned with the influence of finite size effects, in many instances, what one typically uses is a local form of the law, i.e.: $\mathbf{E}(\mathbf{J}) = \rho_0 (J/J_c)^N \mathbf{J}$, and further solves the Maxwell equations by one or another technique [1]. The power-law behavior may be explained as follows. To start

with, in the absence of thermal agitation or other statistical effects, one has the high exponent limit. This fits the so-called critical state regime [2] that describes the sudden transitions of the flux line lattice, avalanching from one configuration to another when the flux pinning threshold is exceeded. Thus, speaking of averaged fields over distances containing a large number of vortices, true superconducting current flow ($E \approx 0$) may occur for the subcritical regime ($J < J_c$ or 'all vortices are pinned'). However, when the critical current density is exceeded, i.e.: $J > J_c$ some equilibrium condition suddenly breaks down and a dissipative regime with a rapid increase of E starts. On the other hand, either related to finite temperatures or to inhomogeneous pinning interactions, a smoothing effect takes place, but remarkably, one can still use a power law dependence, now with a reduced value of N [3]. The validity of the formula over a noticeable range of electric field was explained in [4] through the concept of partial flux flow in the presence of thermal agitation. In practice, one considers it an empirical parameter that may be measured for the material of interest and in the required ambient conditions.

To the moment, the majority of numerical calculations comply with such *power-law* idea and also rely on the so-called *isotropic* hypothesis that follows on the implicit ansatz of parallelism between the vectors **E** and **J**, as indicated before. In fact, as long as the above relation is *scalar*, one can plainly write it in the form $E(J) = \rho_0 (J/J_c)^N J$ that 'cancels out' the corresponding unit vector. Notwithstanding the straightforward explanation of the power-law dependence, the validity of the isotropic behavior is much less clear. Truly, one could find a number of reasons for using this form: (i) its mathematical simplicity, (ii) the fact that, by using a nonlinear resistivity, it is a minimal upgrade of the normal conduction law, and (iii) the satisfactory predictions obtained in many cases, as for long samples in parallel magnetic field. However, contrary to the case of normal conductors, where Ohm's law finds a natural explanation, in type-II superconductivity, unless for the mentioned geometry, with parallel flux tubes, isotropy is not guaranteed. Without going into detail yet, let us just recall that, according to common knowledge, for these materials, the transport properties relate to the drift of the flux tubes under the action of magnetic forces of the kind $\mathbf{J} \times \mathbf{B}$, and this establishes preferential directions in space (in particular those parallel or perpendicular to **B**). Then, one should analyze if the reasonable predictive power of the isotropic law is just a stroke of serendipity for other cases. Even more, it is crucial to detect possible situations in which this ansatz is not acceptable at all. Providing a tool for investigating this fact is the main motivation of our work, that will be outlined below in a simple pictorial way. Other interpretations have been done and will be commented later.

As introduced in previous articles [5], under very general conditions, the **E**(**J**) law threshold for type-II materials with complex flux structures may be described by some closed contour that is formed by the possible values of the critical current density vector (critical points (J_1, J_2) in two-dimensional (2D) problems at some reference frame, as shown in figure 1). At each point of this map, the electric field arising

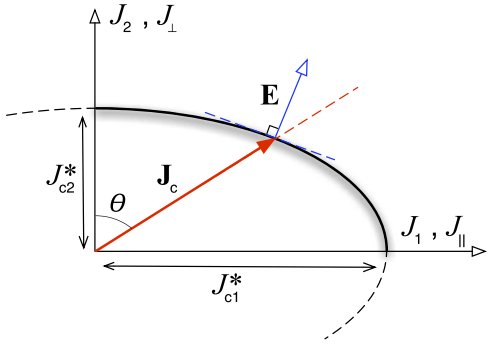

Figure 1. Geometrical interpretation of the **E**(**J**) law in a hard superconductor. The current density takes 'critical' values (J_{c1}, J_{c2}) at some contour, while the electric field points perpendicular to such contour when the equilibrium breaks down and flux flow occurs. In general, the problem is defined within some reference frame in which **J** has the components (J_1, J_2). For homogeneous materials, these components become the projections parallel and perpendicular to the local magnetic field ($J_\parallel$, $J_\perp$).

by the breakdown of criticality points perpendicular to the contour. Recall that, excepting the isotropic case (circular contour) **E** and **J** are no longer parallel unless for the specific cases of **J** pointing along the principal axes. Thus, in practice, the question is to find out whether such a condition is satisfied or not. As we will see, in many experimental instances the answer will be positive (or nearly). This is the case for the vast number of experiments in which a uniform magnetic field of changing modulus is applied either parallel or perpendicular to a flat or very long sample. The screening currents are automatically perpendicular to the magnetic field and the induced electric field parallel to the current density. However, for those cases in which the answer is negative, a component of **J** parallel to the magnetic field appears, and **E** is at an angle with **J**. Then, it will be important to quantify the eccentricity of the critical contour (a 'material' anisotropy of the superconductor under consideration). Apparently, if the semi-axes are similar enough, one could be confident on the predictions made by the isotropic model, that is nothing but the limit in which the contour becomes circular.

In brief, this article brings the practical implementation of the power-law-elliptic model for the **E**(**J**) material law to be used in superconducting application design. It will be derived by combination of the power-law concept and the above introduced contour in the elliptic case. The paper is organized as follows. First, (section 2) we will introduce a physically meaningful reference frame for analyzing the critical current density vector. It is given by the local magnetic field vector and its differential properties. Of particular relevance will be to consider the component of **J** parallel to the magnetic field. Then, in section 3, having clarified the geometry of Ampère's law, we will discuss the relation between the physics of type-II superconductors and the above mentioned elliptic region. We will concentrate on various phenomenological issues related to the accurate determination of the specific elliptic region for a given superconductor from experiment, as well as on the practical expression **E**(**J**). Finally (section 4), in order

to provide some specific tools, as well as for evaluating the relevance of using the correct material law, we give some numerical examples. The discrete version of a variational statement for the power-law-elliptic model is presented and applied to evaluate the transport properties of helical cable inspired configurations. We concentrate on the influence of the basic parameters of the theory: the power law exponent (steepness of the $\mathbf{E}(\mathbf{J})$ dependence), and the eccentricity of the ellipse, given by the ratio between the critical current values at different orientations relative to the local magnetic field.

2. Local geometry of Ampère's law: the normal conducting case

As said before, the relative orientation of the electromagnetic fields $\mathbf{E}$, $\mathbf{J}$, $\mathbf{B}$ in a superconducting material must be considered with care. Unless for the trivial situation in which the magnetic field is confined to one-dimensional (1D) oscillations, one must expect a situation with screening currents not perpendicular to $\mathbf{B}$ and with non-parallel electric fields induced. On the other hand, the selection of an appropriate macroscopic law has to consider intrinsic geometric properties of the electromagnetic fields, together with the constraints introduced by the superconducting interaction. Here, in order to gain understanding of the problem we start by introducing general requirements for the macroscopic fields showing that a natural reference frame may be introduced to visualize the physics beyond the trivial situation $\mathbf{E}\|\mathbf{J}\perp\mathbf{B}$. Then, we will pave the way for the analysis of the superconducting case by first studying the simplest problem of linear materials under the condition $\mathbf{J}\not\perp\mathbf{B}$.

Being interested in the distinction between the component of $\mathbf{J}$ flowing either parallel or perpendicular to the local magnetic field, we introduce a reference frame that, for each point of space relies on the differential properties of the magnetic field. This will be useful for interpretative purposes, as well as for simplifying computations. In practice, the usage of this frame will restrict to situations where distinction between the fields $\mathbf{B}$ and $\mathbf{H}$ is superfluous, i.e.: $\mathbf{B}=\mu_0\mathbf{H}$. So that, no specific consideration is needed for distinction between them.

Consider a generic local magnetic field profile $\mathbf{H}(\mathbf{r})$ around a point P, where generic means that the field is neither null nor constant, and where the gradient of intensity is not aligned with the field, $\mathbf{H}\times\nabla H\neq 0$. Our aim is to identify the correlation between the field and its derivatives with the parallel and perpendicular components of the local current density, according to Ampere's law. We will group these derivatives into mathematically meaningful terms, associated to the geometric profile of the integral lines of $\mathbf{H}$. In order to do this we start by the factorization $\mathbf{H}=H\mathbf{h}$, and consider separately the derivatives of H and of the unit vector $\mathbf{h}$.

Let us choose a cartesian orthonormal basis (named $\{\hat{\mathbf{1}},\hat{\mathbf{2}},\hat{\mathbf{3}}\}$ for generality here) with origin at P, with its first axis along $\mathbf{H}(P)$, the second axis on the plane defined by P, $\mathbf{H}(P)$ and $\nabla H(P)$, and the third axis along $\mathbf{H}(P)\times\nabla H(P)$. Then, we have $\mathbf{H}(P)=H_0\hat{\mathbf{1}}$ and $\nabla H(P)=\partial_1 H|_P\hat{\mathbf{1}}+\partial_2 H|_P\hat{\mathbf{2}}$. Around P we have $\mathbf{H}(\mathbf{r})=H(\mathbf{r})\mathbf{h}(\mathbf{r})$, and we can use spherical angles associated to the reference $\{\hat{\mathbf{1}},\hat{\mathbf{2}},\hat{\mathbf{3}}\}$ to express the unit vector at and around P, such that $\mathbf{h}(\mathbf{r})=\sin\theta(\mathbf{r})\cos\phi(\mathbf{r})\hat{\mathbf{1}}+\sin\theta(\mathbf{r})\sin\phi(\mathbf{r})\hat{\mathbf{2}}+\cos\theta(\mathbf{r})\hat{\mathbf{3}}$, with $\theta(P)=\pi/2$ and $\phi(P)=0$.

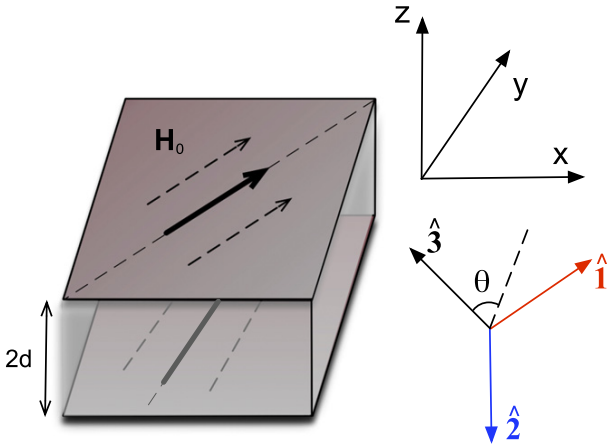

Figure 2. Sketch of the local orthonormal basis $\{\hat{\mathbf{1}},\hat{\mathbf{2}},\hat{\mathbf{3}}\}$ defined in terms of the magnetic field and its derivatives for an infinite slab under parallel magnetic field that changes in modulus and orientation. The dashed line defines the polar angle θ for the magnetic field in the lower plane.

A simple example for visualizing this is the case of an infinite slab with parallel external field (sketched in figure 2). By symmetry, the field is constant (in magnitude and direction) within each parallel plane, so that ∇H must be normal to these planes and $\mathbf{h}$ may rotate in-plane from the surface into the bulk of the sample. In this case, choosing P at the surface and using the global z coordinate to specify the position within the slab: $\mathbf{H}(z=0)=H_0\hat{\mathbf{1}}$, $\mathbf{H}(z)=H_1(z)\hat{\mathbf{1}}+H_3(z)\hat{\mathbf{3}}=H(z)\mathbf{h}(z)$, with $\mathbf{h}(z)=\sin\theta(z)\hat{\mathbf{1}}+\cos\theta(z)\hat{\mathbf{3}}$. The slab approximation is important because it encodes the main behavior of the field in a macroscopic sample, far from corners, edges and curved surfaces. We will use this simplification in several instances along the article.

Let us proceed with the general expression of Ampère's law in our reference frame. By applying $\nabla\times\mathbf{H}=\nabla H\times\mathbf{h}+H\nabla\times\mathbf{h}$, we get

$$\mathbf{J}=-\partial_2 H\hat{\mathbf{3}}+H_0\Big[-\big(\partial_2\theta+\partial_3\phi\big)\hat{\mathbf{1}}+\partial_1\theta\hat{\mathbf{2}}+\partial_1\phi\hat{\mathbf{3}}\Big]. \quad (1)$$

Three different geometric terms can be identified:

(i) $-\partial_2 H\hat{\mathbf{3}}$ will be denoted *screening* of intensity. It is the main component of the perpendicular current density, and appears related to the variations of the field modulus. The screening current is normal to both $\mathbf{H}$ and ∇H, so it is in-plane in the slab approximation.

(ii) $-H_0(\partial_2\theta+\partial_3\phi)\hat{\mathbf{1}}$ represents an *helicoidal* (or torsional) distribution of flux lines around the reference line through P. This term comes from twisted flux lines (curl) along the directions of the unit vectors $\hat{\mathbf{2}}$ or $\hat{\mathbf{3}}$, or a

sum of both. It is the *unique* geometric term of the flux lines correlated to a parallel current density. In the slab approximation it is also in-plane.

(iii) Finally, $H_0(\partial_1\theta\hat{\mathbf{2}} + \partial_1\phi\hat{\mathbf{3}})$ is associated to *bending* of the reference flux line through P, i.e., changes of orientation of the field lines when one 'walks' along them. The rotation of $\mathbf{h}$ can be either in the $\hat{\mathbf{1}}$–$\hat{\mathbf{2}}$ plane (and the term $H_0\partial_1\phi$ is added to the much higher $-\partial_2 H$) or in the $\hat{\mathbf{1}}$–$\hat{\mathbf{3}}$ plane (and $H_0\partial_1\theta$ correlates to a new normal component of the current density orthogonal to the main screening term). Along this article, we will neglect the bending terms to simplify the analysis, understanding that bending is small in the bulk. Indeed, it will vanish exactly in the slab approximation.

The screening current is usually the most relevant in magnitude, with direct physical interpretation as the reaction of the sample against external variation of the magnetic field modulus. Similarly, the helicoidal current is a screening reaction of the sample against external variation (rotation) of $\mathbf{h}$. All this occurs because Faraday's law determines the induction of electric field under variation of magnetic induction. Thus, in a normal metal, parallel and perpendicular components of the electric field generate the corresponding currents. The sample reacts, according to the material law $\mathbf{J} = \sigma_0\mathbf{E}$, against external variations of $\mathbf{H}$.

For a better visualization, we will exploit the planar geometry (see figure 2). Thus, in a slab with field $\mathbf{H}$ parallel to the plane and ∇H perpendicular, there are two independent current densities, screening of field intensity variation and parallel screening of field rotation, both currents in-plane. They will be denoted $\mathbf{J}_\perp = -\partial_2 H\hat{\mathbf{3}}$ and $\mathbf{J}_\parallel = -H_0\partial_2\theta\hat{\mathbf{1}}$.

Let us consider a metallic infinite slab occupying the region $-d \leqslant z \leqslant d$ as sketched in figure 2, that is subject to an excitation of the kind $\mathbf{H}_{\text{applied}} = (H_0 \sin(\omega t), H_0 \cos(\omega t), 0)$. It is well known that, in terms of the normal metal resistivity, the magnetic diffusion equation reads

$$\nabla^2\mathbf{H} = \mu_0\sigma_0\frac{\partial\mathbf{H}}{\partial t}. \tag{2}$$

In figure 3 we visualize the solution of this equation, here for the boundary conditions specified above. For the readers' sake, we recall that a variety of numerical routines are available in different codes that address this problem. In our case, we have adapted a MATLAB function designed to solve the heat equation that formally coincides with ours. Recall that, upon rotation of the applied magnetic field, a peaked structure of parallel screening current appears. The peaks, close to the boundaries of the slab will be a feature later to be observed in superconductors, and clearly ascribed to the lag between internal layers and the rotating boundary condition. This simple example allows analytical manipulations that one can use to better understand the role of $J_\parallel$. Thus, starting with equation (2) it is not difficult to show

$$\mathbf{J}\cdot\mathbf{H} = 0 \Rightarrow \frac{\partial\left(H_x/H_y\right)}{\partial t} = 0, \tag{3}$$

thus ensuring that perpendicularity of $\mathbf{H}$ and $\mathbf{J}$ is only possible for those processes in which field rotation does not occur, as argued before.

We want to emphasize that the above discussion on the appearance of components of $\mathbf{J}$ parallel to the magnetic field is not restricted to linear materials. In fact, it may be extrapolated to the case of nonlinear $\mathbf{E}(\mathbf{J})$ relations and, in particular, to the superconducting power-law. However, specialized numerical methods will be required for the analysis. On the other hand, a relevant distinctive feature for the latter will be the persistent character of the current densities, that only occur as transients in normal metals.

3. E(J) law for type-II superconductors in non-parallel magnetic fields

A simple analysis based on the infinite slab geometry sketched figure 2 together with fundamental concepts of type-II superconductivity will tell us about the specific constraints on any acceptable $\mathbf{E}(\mathbf{J})$ relation when flux rotation occurs. Let us first suppose that $\mathbf{H}_0$ stands for a uniform field applied to the superconducting slab and that the field penetrates in the form of parallel flux tubes. In the standard configuration of a single component field, the following relations hold:

$$\mathbf{B} = B(z)\hat{\mathbf{1}}; \quad \mathbf{J} = J(z)\hat{\mathbf{3}}; \quad \mathbf{E} = E(z)\hat{\mathbf{3}}. \tag{4}$$

For instance, they may be supplemented with a material law of the kind $E = E_0(J/J_c)^N$. Increasing the modulus of $\mathbf{H}_0$ nucleates more and more vortices that penetrate in the sample, driven by the force $\mathbf{J}\times\mathbf{B}$ (along the axis named $\hat{\mathbf{2}}$). Additionally, the electric field and the magnetic flux velocity are connected by the celebrated Josephson's relation $\mathbf{E} = \mathbf{B}\times\mathbf{v}$.

On the contrary, if by virtue of some external process, $\mathbf{B}$ would rotate within the sample, two striking facts need consideration: (i) the rotation of $\mathbf{B}$ would produce a parallel component of $\mathbf{J}$, i.e. J_1 as said in the previous section. Then as long as one has $\mathbf{E}\|\mathbf{J}$ a component of $\mathbf{E}$ parallel to the magnetic field would also appear, a fact that contradicts Josephson's relation. (ii) Contrary to the case for $J_\perp(=J_3)$, an arbitrary value of $J_\parallel(=J_1)$ would be allowed, in a so-called *parallel configuration* equilibrium state. In fact, according to the 'conventional' concept that flux lines drift if required by the magnetic force $\mathbf{J}\times\mathbf{B}$, the parallel condition would result in a force free state with no limit for the supercurrent.

The physical considerations exposed above as well as a number of interesting collateral concepts are already a classical subject. In fact, motivated by the possibility of achieving very high practical critical currents, several decades ago, still in the era of low temperature superconductivity, an intense research activity about the so called 'longitudinal configurations' (in reference to the appearance of $J_\parallel$) has to be reported.

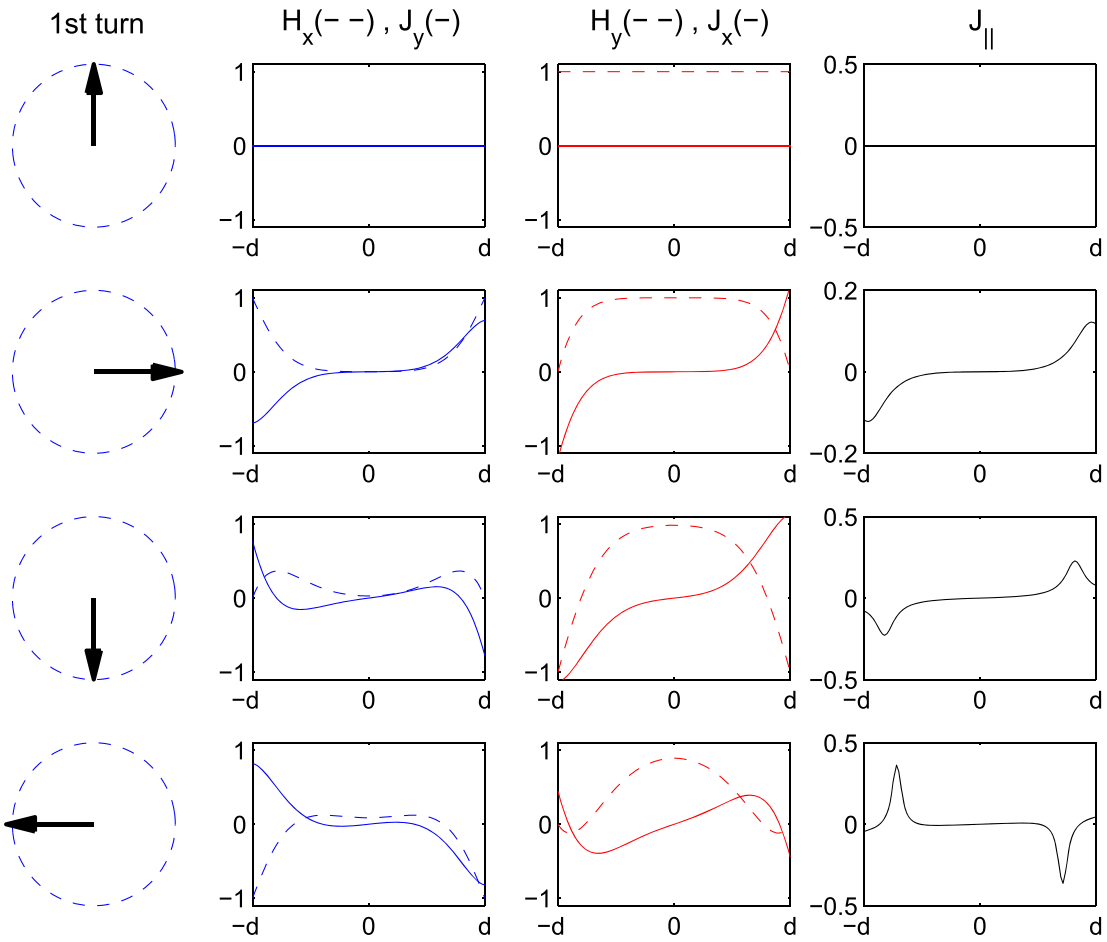

Figure 3. Evolution of the components of **H** and **J** penetrating in a metallic slab (figure 2) as induced by rotation of the applied field. The left column depicts the applied field vector. To the right, we plot the parallel component of **J**. Dimensionless units, defined by the maximum applied field H_{m} and the ratio H_{m}/d have been used.

The interested reader may find some selected contributions to this area, along the years, in [6–15]. As extensively compiled in [16], the main facts can be summarized as follows: (i) in practice, longitudinal configurations are characterized by increased (though finite) values of the critical current $J_{c\parallel}$, (ii) related exotic phenomena as paramagnetic magnetization and negative resistance are found, (iii) a noticeable electric field component along the local magnetic field has been measured, (iv) contrary to the case of $J_{c\perp}$, that is rather well understood in the language of material pinning forces, no consensus exists yet about the real nature of the critical value $J_{c\parallel}$. More in detail, the main topic about the parallel critical current threshold is whether the underlying physical mechanism is flux cutting (as considered for a long time) or not. Contrary to such hypothesis are the facts that concomitant theoretical predictions greatly overestimate the measured values of this quantity and also the experimental observation that $J_{c\parallel}$ is noticeably influenced by the pinning center landscape [16]. Moreover, as shown in that reference, if one completes the theory with the concept of pinning torque balance, a reasonable prediction for the parallel critical current threshold is obtained, together with a natural upgrade of Josephson's relation $\mathbf{E} = \mathbf{B} \times \mathbf{v} + \nabla\Psi$.

Below, we will describe our geometrical interpretation of the general critical current problem, including the perpendicular as well as the parallel component of $\mathbf{J}_c$. The equivalence to the description by Matsushita [16] will be established. Eventually, we will introduce the description of the resistive regime, i.e.: the $\mathbf{E}(\mathbf{J})$ law dealing with the *overcritical* behavior.

3.1. Geometrical formulation of the critical state: critical current yield region

As introduced before, figure 1 gathers the main features of our critical state theory for general problems with $J_{c\parallel}$ and $J_{c\perp}$ contributing at any relative strength [17]. Recall that the equilibrium 'critical states' of the superconductor are given by a certain 'yield region' defined by the admissible endpoints of the critical current density vector $\mathbf{J}_c$. Under a certain external process, that induces an instantaneous overcritical condition, $\mathbf{J}_c$ moves to another point of the locus, and the updated equilibrium is defined by the condition that the transient

electric field is perpendicular to the contour. No further evolution along the perfectly conducting contour occurs because along such boundary one has $\partial_t \mathbf{J} \propto \mathbf{E}$. On the other hand, the actual shape of the 'critical' $J_{c\perp}(J_{c\parallel})$ curve is dependent on the underlying physics:

- if one assumes that $J_{c\parallel}$ and $J_{c\perp}$ are governed by different physical phenomena (as in the cutting/pinning hypothesis) the region is a rectangle limited by the points $(\pm J^*_{c\parallel}, \pm J^*_{c\perp})$, with $J^*_{c\parallel}$ and $J^*_{c\perp}$ being independent material parameters. This approximation corresponds to the well-known double critical state model [14], that has been extensively exploited.
- If one assumes that $J_{c\parallel}$ and $J_{c\perp}$ relate to the same physical mechanism, a certain functional relation $J_{c\perp}(J_{c\parallel})$ may be established, and one has a contour defined by some smooth curve. This idea supports the elliptic models [20], a class that includes our current proposal.

Let us show that, if one follows the simplifying ansatz that it is one single physical mechanism that fully determines the constraint forces that hold flux structures in equilibrium [16], then, the yield region is an ellipse. Although a rigorous treatment of vortices and their interactions would require to invoke the Ginzburg–Landau theory, the London approximation will suffice for incorporating the relevant ideas. Thus, to start with, we consider that magnetic flux penetrates the superconductor in the form of a net of straight, rigid flux tubes (vortices) interacting with each other, with the magnetic field, and possibly with the underlying material. A somewhat lengthy but standard calculation gives the following expression for the vortex lattice free energy, under the action of an external field [18, 19]

$$\mathcal{G}_V = \Phi_0 \left[-\sum_p H_0\, l \cos\left(\beta_p\right) + \frac{\Phi_0}{\mu_0 \lambda} \sum_{p<m} \cot\left(\beta_p - \beta_m\right) \times \exp\left(-d_{pm}/\lambda\right) \right]. \tag{5}$$

Here, β_p is the tilt angle for the vortex p relative to the external field direction and d_{pm} the (minimum) distance between the vortices p and m.

What is important here is to realize that for large magnetic fields H_0 (as compared to the field created by the vortices themselves at each point of space) the dominant term for each individual vortex is $H_0 \cos(\beta_p)$, and the stationary array is the well known arrangement of parallel vortices: $\beta_p = 0$, $\forall p$ in a regular triangular mesh. On the other hand, in the presence of pinning, stationary configurations of magnetic field with non-vanishing current density components, both perpendicular (gradient of field intensity) and parallel (lack of alignment) may exist. One can say that the vortex–vortex and vortex–external field interactions are balanced by some 'vortex-pin' force and then: (i) the perpendicular component of the local current density is maintained in the stationary regime by a pinning force opposed to the repulsion between vortices. Similarly, (ii) the parallel component of the current density, associated to misalignment of flux lines with the external field, is maintained by an opposed pinning torque. This is sketched in figure 4. The reader is addressed to [16] for a detailed discussion on the physical origin of torques.

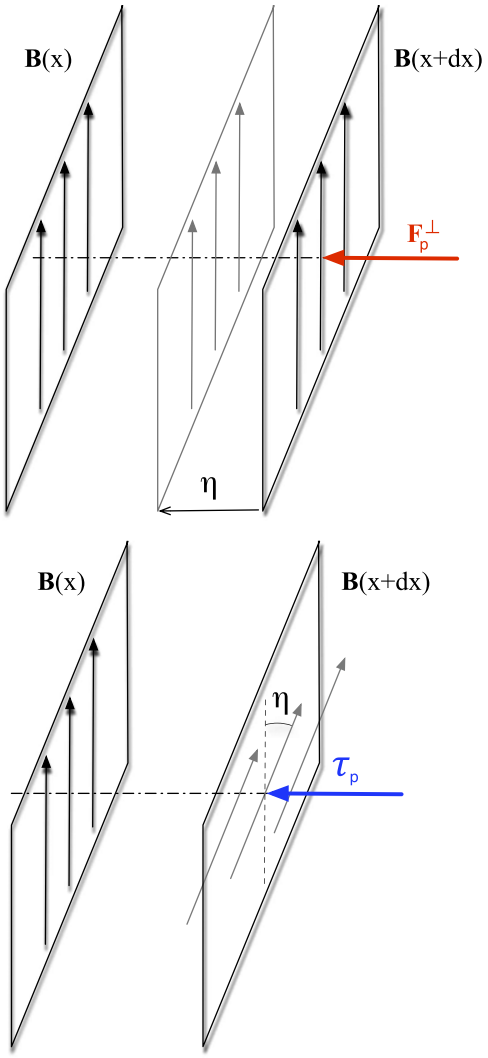

Figure 4. Sketch of virtual perturbations of the flux line lattice relative to the configuration of equilibrium. Upper: compression of flux lines. Lower: rotation. Also indicated are the pinning actions against the restoring forces.

In this scenario, the thresholds for the two components of $\mathbf{J}_c$ are related to the projections of a unique pinning force vector, say $\mathbf{F}_0$ either parallel or perpendicular to the plane of the slab under consideration: $\mathbf{F}_0 = (F_0 \sin(\varphi), F_0 \cos(\varphi)$. Assuming linearity in the relation between the forces (torques) and the current densities, that is to say: $J_{c\parallel} = c_1 F_0 \cos(\varphi)$, $J_{c\perp} = c_2 F_0 \sin(\varphi)$ one arrives at the equilibrium condition

$$\left(\frac{J_{c\parallel}}{c_1 F_0}\right)^2 + \left(\frac{J_{c\perp}}{c_2 F_0}\right)^2 = 1, \tag{6}$$

where c_1 and c_2 play the role of phenomenological constants,

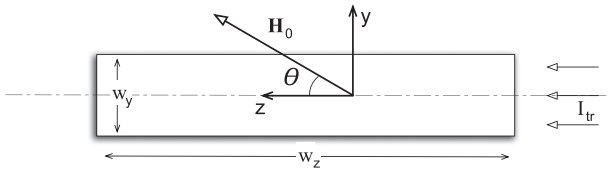

Figure 5. Sketch of the experimental setup used for obtaining the critical current density yield region as a function of the angle between **J** and the magnetic field. In this case ($w_x \ll w_y \ll w_z$), **J** is basically along z-axis and the self field can be neglected. $\mathbf{H}_0$ stands for the applied magnetic field.

allowing different critical parameters $J^*_{c\parallel} = c_1 F_0$, $J^*_{c\perp} = c_2 F_0$, and thus, magnetic anisotropy[3].

In conclusion, the common origin of a total threshold for pinning interaction forces and torques which balance the intrinsic repulsion and alignment, gives way to an elliptic region of critical supercurrents at each point of the sample, with principal axis parallel and perpendicular to the local field. Obviously all this refers to the mesoscopic scale, i.e.: after coarse graining in order to smooth fluctuations in the scale of individual vortices.

3.2. Experimental determination: securing the $\{J_{c\perp}, J_{c\parallel}\}$ relation

The investigation of general critical states has deserved attention in numerous experiments in the last decades, but it has not been until recently that a clear evidence of the kind of mechanism controlling $J_{c\parallel}$ and $J_{c\perp}$ has been available. The relevance of parallel current flow in type-II superconductors was been tested in a dedicated experiment [20] that, provides direct information on the threshold (critical) current density when **J** and **B** are at an arbitrary angle.

Figure 5 displays the basic features of the experimental setup. Owing to the quasi-1D structure of the conductor, and to the negligible self-field effects, the authors could draw a clear picture of the critical current behavior, i.e.: $\mathbf{J}_c(\theta)$. Based on the straightforward measurement of the voltage in their transport measurement, they present a set of data for the induced electric field components $E_y(\theta)$ and $E_z(\theta)$. As a figure of merit, that allows to clearly distinguish between different models, they plot the ratio $E_y(\theta)/E_z(\theta)$. Basically, the experimental data agree with a dependence of the kind $[(1-a^2)\tan(\theta)]/[a^2+\tan^2(\theta)] \equiv \Phi_c(a,\theta)$ with a some constant, as will be later discussed. Such data, supported by complementary analysis by Campbell [21] together with diverse publications that focus on the angular dependences [22] confirm that an elliptic *yield* region

$$\frac{J_c^2\cos^2(\theta)}{J^{*\,2}_{c\parallel}} + \frac{J_c^2\sin^2(\theta)}{J^{*\,2}_{c\perp}} = 1 \tag{7}$$

is an excellent approximation to the dependence $\mathbf{J}_c(\theta)$. As noticed by the authors, although the transport measurement provides a direct information as relates the direction of the current density vector, one has to be careful with the voltage criterion that are used for determining the 'critical' components. In their experiment, the determination of the $J_{c\perp}(J_{c\parallel})$ critical curve was secured by checking the independence of the results when changing the threshold. Here, we add some theoretical analysis that gives another perspective of the problem. The question is that transport measurements rely on the detection of a voltage when the system is driven away from equilibrium ($\mathbf{J}_c \to \mathbf{J}_c + \Delta\mathbf{J}$) and one is just willing to reconstruct the equilibrium region $\mathbf{J}_c(\theta)$. Taking advantage of the quasi-linear analysis developed in [5] we have derived the following expression that quantifies the deviation of the measured critical curve in terms of the voltage criterion:

$$j_0(\theta,\delta,\Gamma_0) = j_c(\theta,\Gamma_0) + \delta_\perp\Big[1 + \Phi_c\, j_c^2\sin\theta\cos\theta\left(1-\Gamma_0^2\right) - j_c^3\left(\Gamma_0^3\cos^2\theta + \sin^2\theta\right)\Big]. \tag{8}$$

Here, we have introduced the dimensionless parameters $\delta_\perp = E_0/(\rho_0 J_\perp)$, that quantifies the voltage criterion, $j_c = \sqrt{(1+\tan^2\theta)/(\Gamma_0^2+\tan^2\theta)}$, and $\Gamma_0 = J^*_{0\perp}/J^*_{0\parallel}$. The subindex '$_0$' is used to indicate 'measured values' by contrast to their ideal counterpart '$_c$'. Notice that the above expression may be used for testing the influence of the voltage criterion in the determination of the yield region, more specifically, one can check the anisotropy ratio obtained from experiment. Figure 6 displays its application by the 'reconstruction' of the yield region for different values of the anisotropy parameter and voltage criterion used. It is apparent that deformation of the reconstructed contour increases with the voltage criterion, as well as with the actual anisotropy ratio. As one could expect the more isotropic the behavior, the less relevant the threshold used.

Enlightened by these above discussion, our contribution proceeds as follows. Having established that the elliptic region is privileged both theoretically and from experiments, we will subsequently introduce an discuss a tractable form of the related $\mathbf{E}(\mathbf{J})$ law to be used in calculations, and eventually show some numerical applications.

3.3. The critical 'yield region' and the $\mathbf{E}(\mathbf{J})$ law

Having established that an elliptic region of supercurrents is a proper description of the threshold against general distortions of the flux line lattice, our next step is to investigate the overcritical behavior. Physically, the situation is as follows. We start from the basic knowledge that in 1D situations (those problems for which $J_\parallel = 0$ is guaranteed) perturbations are described by an 'almost vertical' $\{E, J\}$ graph with associated equilibrium condition $J = J_c$ (or 0). In counterpart, for a

[3] The components of the current density vector characterizing the equilibrium state are labelled with a subindex 'c': $\mathbf{J}_c(\theta) \equiv (J_c\sin\theta, J_c\cos\theta) \equiv (J_{c\parallel}, J_{c\perp})$. This set of points defines the critical yield region. On the other side, the parameter values that quantify a specific curve are marked with an asterix. Thus, for the elliptic case, $J^*_{c\parallel}$, $J^*_{c\perp}$ define the semi-axis.

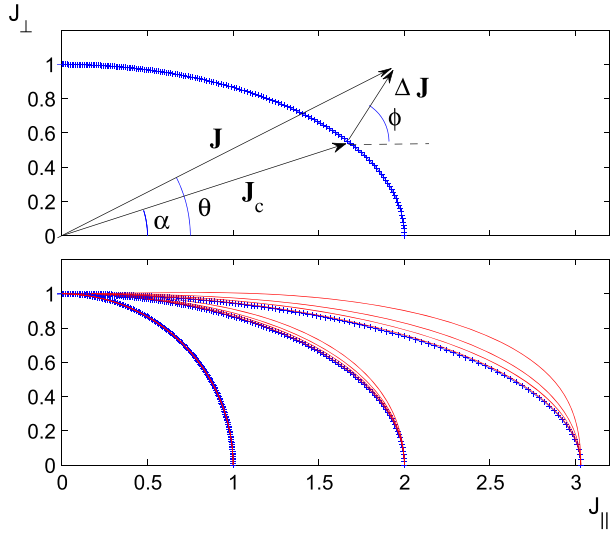

Figure 6. Model test of the voltage criterion effect on the reconstruction of the critical current yield region. The upper panel is a sketch the overcritical current (**J**) that relates to the experiment, as well as the corresponding 'real' critical current density $\mathbf{J}_c$. The lower panel shows the actual reconstruction of the critical curves when different voltage criteria δ are used. Specifically, we plot the profiles coming from the set of values $\delta = 0.01, 0.05, 0.1, 0.2$ and for the anisotropy ratios $\Gamma = 1, 0.5, 0.33$. For each value of Γ, deformation of the ideal elliptic profile (crosses) increases with δ.

general situation, criticality will be expressed by $\mathbf{J} \in \Omega_c$ (or 0) with Ω_c the elliptic contour mentioned before. Previously [5], we argued that transients from overcritical points back towards the region Ω_c could be described by a thermodynamic dissipation function $\mathcal{F}$. This function measures the entropy production and, to the lowest order, is quadratic in the separation from equilibrium ΔJ. In addition, it was shown that the electric fields along the dissipative process may be obtained as $\mathbf{E} = \nabla_{\mathbf{J}}\mathcal{F}$.

Below, we develop the theory for the power-law extension beyond the elliptic critical state region. In brief, this entails to identify a mathematical expression for $\mathcal{F}$ that introduces a power-like penalty when **J** goes beyond the boundary Ω_c (see figure 6 for a sketch of the situation). Other meaningful expressions for $\mathcal{F}$ as the plain parabolic behavior have been checked, but will be discussed elsewhere.

*3.3.1. Elliptic-power-law **E(J)**.* The starting point for the elliptic-power-law model is the following expression for the dissipation function

$$\mathcal{F}_{\mathrm{PL}}(\mathbf{J}) = \mathcal{F}_0\left[\left(\frac{J_{\parallel}}{J^*_{c\parallel}}\right)^2 + \left(\frac{J_{\perp}}{J^*_{c\perp}}\right)^2\right]^M. \tag{9}$$

At this point $\mathcal{F}_{\mathrm{PL}}(\mathbf{J})$ is introduced as a reasonable assumption of a mathematically tractable model that accounts for dissipation when the critical condition represented by equations (6) and (7) is overpassed. A complete theory relating the value of M to the flux-pinning properties is out of reach here. However, it will be shown that some physical observables (as the actual angle between **E** and **J**) are indeed model-independent. Notice also that the 'partition' of energy dissipation is ensured because by means of the 'penalty function' in equation (9) one accounts for virtual displacements (figure 6) that can be decomposed as the sum of parallel and perpendicular components, at least differentially. Again, this relies on the idea that a single physical mechanism (flux depinning) is the basic limitation for either conventional or longitudinal configurations. On the practical side, taking derivatives as dictated by $\mathbf{E} = \nabla_{\mathbf{J}}\mathcal{F}$ along the principal directions, one may easily obtain

$$\mathbf{e}(\mathbf{j}) = \left(j^2 + \gamma\, j_{\parallel}^2\right)^{M-1}\left(\mathbf{j} + \gamma\, \mathbf{j}_{\parallel}\right). \tag{10}$$

This formula is a central result of our work, and will be discussed in detail below. Firstly, dimensionless units have been introduced for convenience, through the definitions

$$\begin{aligned} &\gamma \equiv {J^*_{c\perp}}^2/{J^*_{c\parallel}}^2 - 1 \equiv \Gamma_c^2 - 1, \\ &\mathbf{j} \equiv \mathbf{J}/J^*_{c\perp};\ \ \mathbf{j}_{\parallel} = j_{\parallel}\mathbf{h}, \\ &\mathbf{e} \equiv \mathbf{E}/\left(2M\mathcal{F}_0 J^*_{c\perp}\right). \end{aligned} \tag{11}$$

Recall that the anisotropy constant has been reformulated in terms of the new parameter γ, with the purpose of achieving a compact and meaningful final form for the electric field **e**. Thus, one can notice that

(i) the isotropic law, i.e. $\mathbf{e}(\mathbf{j}) = j^{2M-1}\hat{\boldsymbol{j}}$ is obtained in the limit $\gamma \to 0$ as expected.
(ii) In those problems for which the parallel current flow may be neglected ($j_{\parallel}/j_{\perp} \to 0$) one also recovers the formula $\mathbf{e}(\mathbf{j}) = j^{2M-1}\hat{\boldsymbol{j}}$ (*pseudo*-isotropic situation).

As a consistency check, one may calculate the angle between the electric field (normal to $\hat{\phi}$) and the current density (normal to $\hat{\alpha}$), just by starting with equation (10) and applying

$$\cos(\phi - \alpha) = \frac{\mathbf{e}\cdot\mathbf{j}}{|\mathbf{e}|\,|\mathbf{j}|}. \tag{12}$$

Then

$$\tan(\phi - \alpha) = \frac{\left(1 - \Gamma_c^2\right)\tan(\alpha)}{\Gamma_c^2 + \tan^2(\alpha)}. \tag{13}$$

Noticeably, this expression coincides exactly with the expression that was earlier derived for the quasi-linear model [5], and also with the experimental observation reported in [20]. What is more, the angle between the electric field and the current density happens to be independent of the power law exponent M.

4. Numerical application: examples

In this section, we take a step further in the validation of the elliptic-power-law characteristic. Several numerical examples

will be provided, for which the existence of parallel current flow is relevant. To start with, we will consider the longitudinal problem in a strip (experimental setup of figure 5) but now with the inclusion of a finite width. Secondly, a stack geometry with different directions for the transport current along each element, will be studied, aiming at the basic description of helical cable structures. Such configurations have been extensively treated in the literature [23, 24], but as it will be seen below, noticeable effects due to the appearance of parallel current flow may occur, that introduce corrections to the isotropic modelling.

4.1. Quasi-1D analysis of the transport measurements determining $\mathbf{J}_c(\theta)$

The analysis of the transport problem described in figure 5 was done under the 1D condition $w_x \ll w_y \ll w_z \Rightarrow \mathbf{J} \approx J_0\hat{\mathbf{z}}$. Here, we will still consider a long and thin sample, but allow the appearance of local effects across the width, i.e.: we solve the transport problem modelled by

$$\begin{aligned} &\mathbf{J} \approx J_z(y)\hat{\mathbf{z}} \\ &J_{\parallel} = J_z(y)h_z(y) \\ &J_{\perp}^2 = J_z^2(y)\Big(1 - h_z^2(y)\Big). \end{aligned} \tag{14}$$

Here, $h_z(y)$ is the z-component of the unit vector pointing along the full magnetic field $\mathbf{H} = \mathbf{H}_0 + \mathbf{H}_{\rm self}$. Apparently, the correction to the 1D solution will be more important close to the edges, where the self field effects are more influent on the local magnetic field orientation. As said before, an iterative method can be used to solve for the y-dependence of $\mathbf{H}_{\rm self}$, arising from the distribution $j_z(y)$ itself.

Starting from our previous work [5] in which we applied the power-law to the *pseudo*-isotropic situation $\theta = 90° \Rightarrow J_{\parallel} = 0$, here we expand the result to the range $0 < \theta < 90°$. The numerical method described in that work (equations (25) and (26)) has been applied for a dissipation function that now reads

$$\mathcal{F} = \mathcal{F}_0\Big(1 + \gamma\, h_z^2\Big)^M J_z^{2M}. \tag{15}$$

In discrete form, h_z and J_z are evaluated at a collection of segment coordinates $\{y_i\}$, $i = 1, \ldots N$ with $y_1 = -w_y/2, \ldots, y_N = w_y/2$. This parametrizes a collection of long parallel straight wires, each carrying a current I_i. We have investigated the resistive transition in terms of the angle θ, by imposing the evolutionary transport condition

$$\sum_i I_i\big(t, \theta_0\big) = I_{\rm tr}\,\big(t, \theta_0\big), \tag{16}$$

with $I_{\rm tr}\,(t, \theta_0)$ the increasing value of the transport current at a given angle θ_0 with the applied field. Figure 7 shows the main features of our results for $\Gamma_c = 1/3$, the actual value reported in [20]. (i) To the left, we plot the sheet current profiles that appear for the extreme condition $\theta = 0$. Notice the increase of the transport current density allowed towards the center of the sample. This may be explained in terms of zones where parallel transport is enhanced. For the smaller applied fields ($H_0 = 5H_c$ here), one can see that previous to the full penetration regime, a peak may occur, as an indication of the locus of maximum $J_{\parallel}$. For the case $H_0 = 50H_c$, the current flow is basically longitudinal all across the width. (ii) Another aspect that has to be recalled is the robust behavior of the anisotropy dependent quantity $\langle E_y\rangle/\langle E_z\rangle$ against the applied angle. Thus, in spite of the noticeable influence of the voltage criterion in the actual values of $\langle E_y\rangle$ and $\langle E_z\rangle$, the ratio between them accurately follows the ideal behavior given by the 1D relation (equation (13)) for a wide range of transport levels along the sample.

4.2. Approximation to the helical cable: modelling by planar stacks

Being interested in modelling devices with superconducting currents flowing along various regions of space, we start by considering the functional analysis problem introduced in [5, 25]. Under magneto-quasi-static conditions, any electromagnetic process, initiated by manipulation of the sources, may be solved by minimization of the functional

$$\begin{aligned} \langle\hat{L}\rangle_{\rm dis}[\mathbf{J}] = &\int_V\int_V\left[\frac{\mathbf{J}_{n+1}(\mathbf{r})\cdot\mathbf{J}_{n+1}(\mathbf{r}')}{\|\,\mathbf{r}-\mathbf{r}'\|} - 2\frac{\mathbf{J}_n(\mathbf{r})\cdot\mathbf{J}_{n+1}(\mathbf{r}')}{\|\,\mathbf{r}-\mathbf{r}'\|}\right] \\ &+ \frac{8\pi}{\mu_0}\int_V\Big(\mathbf{A}_{{\rm e},n+1} - \mathbf{A}_{{\rm e},n}\Big)\cdot\mathbf{J}_{n+1} \\ &+ \frac{4\pi\Delta t}{\mu_0}\int_V\mathcal{F}\Big(J_{\parallel,\,n+1},\, J_{\perp,n+1}\Big). \end{aligned} \tag{17}$$

Here, the subindex 'n' indicates the value of the quantity for the time layer t_n, Δt is the time interval ($\Delta t \equiv t_{n+1} - t_n$) and $\mathbf{A}_{\rm e}$ stands for the vector potential related to the external sources. Formally, the problem to be solved is: find the vector field $\mathbf{J}_{n+1}$ (the current density distribution) that minimizes $\langle\hat{L}\rangle_{\rm dis}$ subject to the constraints and boundary conditions (in particular, the values at previous time layer $\mathbf{J}_n$). The additional transport prescription $\int\mathbf{J}\cdot{\rm d}\mathbf{s} = I_{\rm tr}$ will have to be applied if electric current is fed through the superconductor. Recall that the notation $\langle\hat{L}\rangle_{\rm dis}$ is a reminder of the background of the theory: we rely on a modified electromagnetic field Lagrangian, as discussed in [5, 25]. Recall also that, the elliptic-power-law will be introduced through the specific selection of $\mathcal{F}$.

In this section, we have developed the numerical application of equation (17) for the geometry described in figure 8. As a first approximation to the helical geometry, we introduce a planar model that allows a conceptual understanding, as well as some simple tests against analytical evaluation. Nevertheless, upgrading to the actual cylindrical geometry is straightforward as will be explained below.

To start with, we notice that as explained by Clem and Malozemoff [24] the inner and outer layers may be solved separately in this problem. In fact, the coupling between them only occurs through a global factor, which is the magnetic field in the intermediate region. This quantity is only dependent on the net currents within each superconductor, and not on the actual distribution $\mathbf{J}(z)$. Let us, thus, concentrate on the

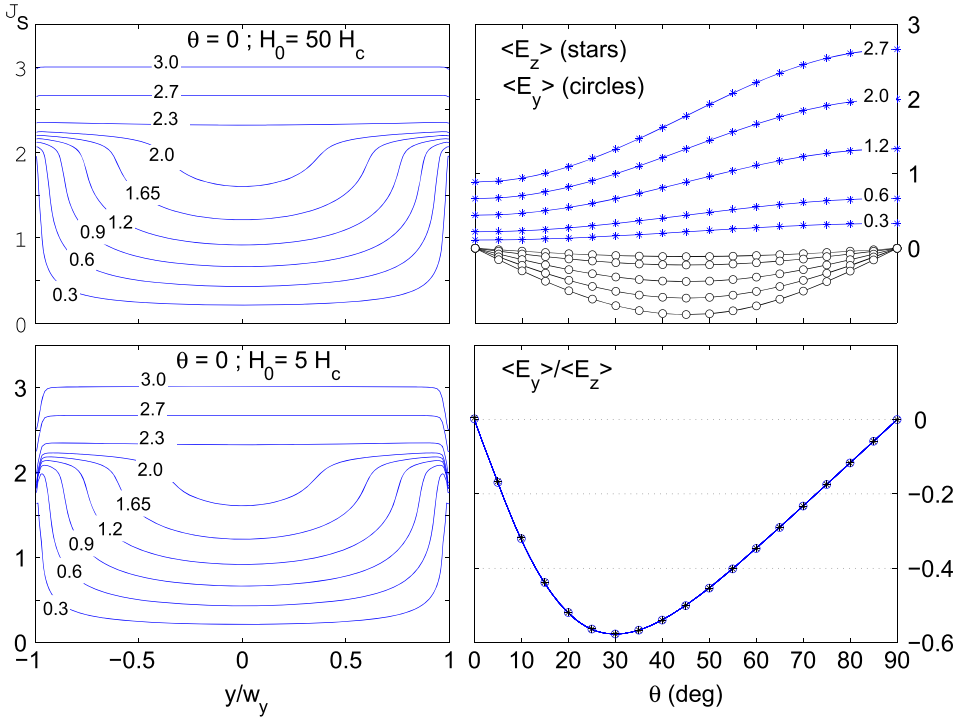

Figure 7. Application of the elliptic power-law model to the experiment sketched in figure 5 in the case of a finite width sample under a moderate applied magnetic field at an angle. To the left, the sheet current density across the width of the sample w_y. Labels indicate the increasing values of the transport current in normalized units ($J^*_{c\perp} w_x w_y$). Also, we use $H_c \equiv J^*_{c\perp} w_x/\pi$. To the right, we show the average electric fields and their ratio as a function of the angle between field and current. The upper pane shows each component at different values of the transport current. All curves collapse when one plots their ratio (lower pane) and converge to the 1D relation in equation (13).

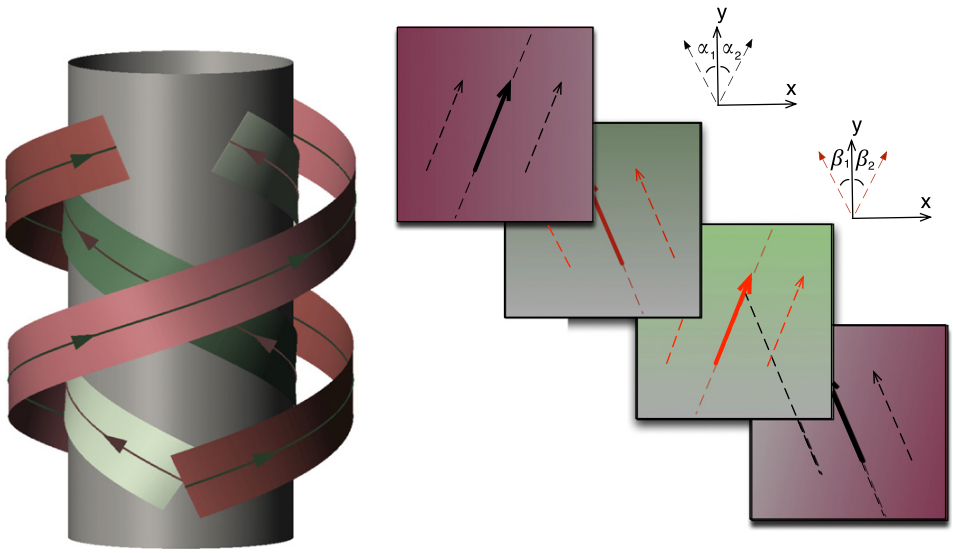

Figure 8. Left: sketch of a two-layer counter-wound cylindrical cable built from superconducting tapes. Right: approximation to the cable geometry by a stack of infinite slabs.

outer layers. Due to symmetry, one can just solve one of the two slabs (for instance the upper one in our plot). By using the coordinates defined in the figure, we state the problem as follows:

We want to solve equation (17) for a thick slab occupying the region $0 < z < d$ (i.e.: V), carrying a transport current $I_{\rm tr}$ along the axis $(\sin\alpha_1, \cos\alpha_1, 0)$, and coupled to: (i) an identical slab with transport along $(-\sin\alpha_2, \cos\alpha_2, 0)$,

and (ii) the field created by two inner slabs also carrying I_{tr} each, but at the angles β_1 and $-\beta_2$ as shown in figure 8.

This will be done by numerical minimization of the following expression, that is the discrete counterpart

$$\langle \hat{L} \rangle_{dis}\left[\{I_i^x, I_i^y\} \right] = \frac{1}{2}\sum_{i,j} I_i^x \mathcal{M}_{ij}^x I_j^x - \sum_{i,j} \tilde{I}_i^x \mathcal{M}_{ij}^x I_j^x + \sum_i I_i^x \left(A_e^x - \tilde{A}_e^x\right) + \frac{1}{2}\sum_{i,j} I_i^y \mathcal{M}_{ij}^y I_j^y - \sum_{i,j} \tilde{I}_i^y \mathcal{M}_{ij}^y I_j^y + \sum_i I_i^y \left(A_e^y - \tilde{A}_e^y\right) + \mathcal{F}_0 \Delta t \sum_i \left[\left(\frac{I_i^{\parallel}}{I_{c\parallel}^*}\right)^2 + \left(\frac{I_i^{\perp}}{I_{c\perp}^*}\right)^2 \right]^M. \quad (18)$$

Here, we have used the discretization of V in the form of a set of parallel layers, each at the position z_i, with $z_1 = 0, ..., z_N = d$ and constant thickness $\delta = d/N$. The layers may carry current along the x and y axes. In fact, we have defined the sheet currents along the cartesian axes $I_i^x \equiv J_x(z_i)\delta$ and $I_i^y \equiv J_y(z_i)\delta$ (our set of $2N$ unknowns). Also included is the coupling to the applied vector potential $A_e^{x,y}$. Tilded quantities refer to the previous time layer. Dissipation within each sheet is parameterized by the function F_i that depends on the current components $I_i^{\parallel}$ and $I_i^{\perp}$. Recall that, for each time step, the evaluation of parallel and perpendicular components is performed multiplying by the previous local magnetic field, i.e.:

$$\begin{aligned} I_i^{\parallel} &= I_i^x \tilde{h}_i^x + I_i^y \tilde{h}_i^y, \\ I_i^{\perp} &= I_i^x \tilde{h}_i^y - I_i^y \tilde{h}_i^x \end{aligned} \quad (19)$$

with $\tilde{\mathbf{h}}_i$ the unit vector along the magnetic field at z_i from the previous iteration. This quantity must be updated for each time step, by application of Ampère's law.

Finally, we have to notice that the 'mutual inductance coefficients' between the layers $\mathcal{M}_{ij}$ must be dealt with care in this problem. In fact, with our selection of axes, together with the specific orientation for the transport current, one has

$$\begin{aligned} \mathcal{M}_{ij}^x &= 1 + 2[\min\{i,j\}] \qquad i \neq j, \\ \mathcal{M}_{ii}^x &= 2\left(\frac{1}{4} + i - 1\right), \\ \mathcal{M}_{ij}^y &= 1 + 2[N - \max\{i,j\}] \quad i \neq j, \\ \mathcal{M}_{ii}^y &= 2\left(\frac{1}{4} + N - i\right). \end{aligned} \quad (20)$$

As it was discussed in [17], the different expressions have to do with the symmetry/antisymmetry conditions for the current flow along each direction. On the other hand, application to the cylindrical geometry would merely consist of replacing these expressions for planar layers by their counterparts, i.e.: either longitudinal or azimuthal current tubes.

4.3. Approximation to the helical cable: results

The solution of the problem stated in equation (18) has been studied in terms of the main parameters of the elliptic power law model, i.e.: the exponent M and the anisotropy ratio $\Gamma = J_{c\perp}^*/J_{c\parallel}^*$. Realistic values in the range of those for HTS at liquid nitrogen temperature have been used. In particular, we have explored the influence of the power M between 10 and 100, and compared the isotropic hypothesis ($\Gamma = 1$) to the values $\Gamma = 1/2$ and $\Gamma = 1/4$ that are close around $\Gamma \approx 1/3$ obtained in [20] for a patterned YBCO film. Our main findings are summarized in figures 9–12.

4.3.1. Influence of the power law exponent M. Figure 9 shows a collection of two dimensional maps that, on the one side assess the validity of our numerical method. Notice that, as expected, the dissipation function restriction introduced in our variational model, gives place to a concentration of points close around the elliptic (in this case, circular) yield region. The higher the value of M, the narrower the region 'explored' by the sample, eventually becoming a thin line when in the critical state limit ($M \gg 1$). On the other side, one can also realize that the appearance of dissipation produces distinctive features in the $[\parallel, \perp]$ or $[x, y]$ plots. In the former case, the states beyond *full penetration* (i.e.: the critical current has been exceeded) are characterized by a narrow band of values of constant $\mathbf{J}$ modulus that rotates as M increases. In the $[x, y]$ plots, the concentration of *overcritical* points appears around the vertical axis (along which transport was addressed in this case).

4.3.2. Influence of the anisotropy parameter Γ. Two aspects have been analyzed as regards the influence of the ratio between the parallel and perpendicular critical current values $\Gamma = J_{c\perp}^*/J_{c\parallel}^*$. Firstly, as shown in figure 10, we concentrate on the magnetic hysteresis loops predicted for the currents circulating along the outer superconducting layer. The main purpose of this simulation was to evaluate how strongly anisotropy affects the shapes of the loops and, as a consequence, the electromagnetic losses. In particular we have evaluated the magnetic moment per unit area of the slab as

$$\mathbf{m} = \int_0^d z \times \mathbf{J} dz. \quad (21)$$

A number of distinctive features are to be recalled for the ac process generated by the transport current cycle $I_{tr} = I_0 \sin(\omega t)$.

(i) Only for the case $\Gamma = 1$ a collapse of the loop m_x is observed. The absence of hysteresis indicates that the profile of current density has reached the dissipation limit, i.e.: $\mathbf{J} - \mathbf{J}_c$ lies beyond the contour Ω_c all around the material.

(ii) The anisotropic cases show a feature in the form of a kink in the loops, that shows up close to the condition $I_{tr} = 0$. This feature is a clear indication of the increased value of $J_{\parallel}$ and thus can be used as a test of

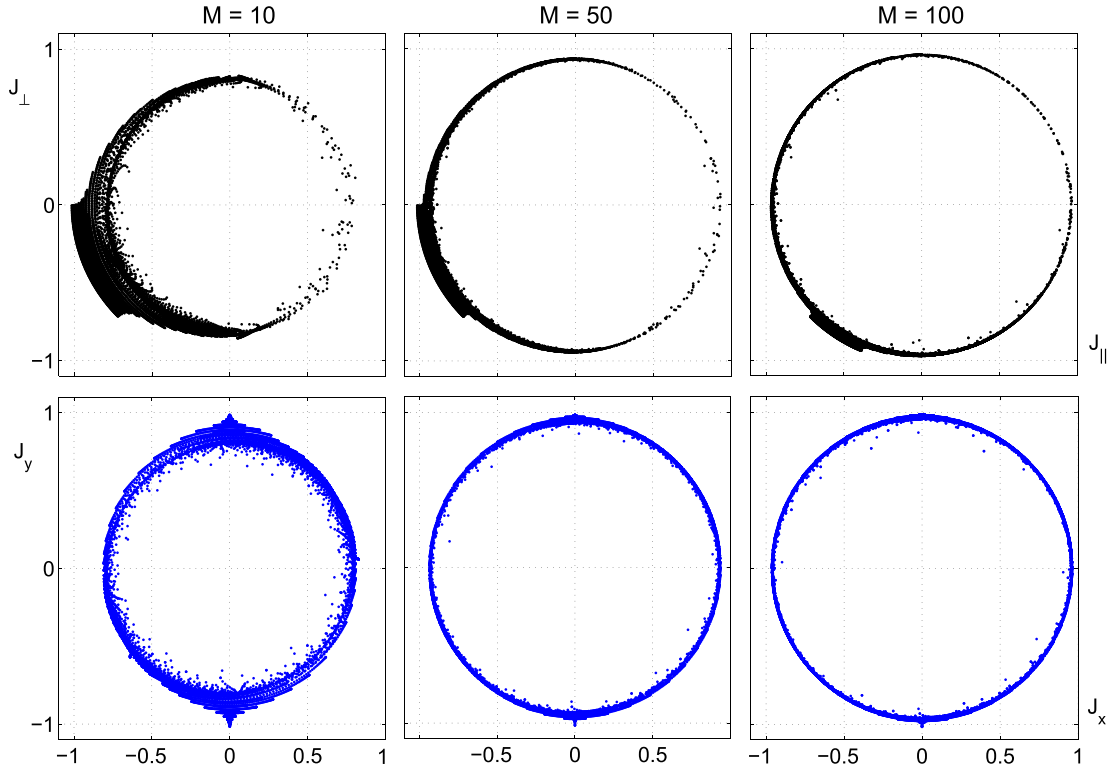

Figure 9. 2D plot of the region 'explored' by the superconducting slab (figure 8) that is fed through with an ac transport current of amplitude $I_{\mathrm{tr,\,max}} = I_c$. Each dot represents a point in **J**-space that has occurred somewhere within the material. The upper plots correspond to the local axes relative to the field direction and its normal [||, ⊥]. The lower pane shows the counterpart for the same conditions, but in terms of the global [x, y] components. Each column corresponds to a given value of the exponent M as labelled. In all cases, the isotropic condition $\Gamma = 1$ was used. For this simulation, the angles defined in figure 8 take the values $\alpha_1 = \alpha_2 = 0$ and $\beta_1 = \beta_2 = 90°$. **J** is given in units of $J^*_{c\perp}$.

the appearance of intrinsic anisotropy Remarkably, such behavior was reported in early experiments with longitudinal fields [26]. In order to clarify this interpretation we include a plot of the components of **H**, as well as the profiles of **J** (figure 11). The reader may notice the increased shielding (higher slope of $h_x(z)$) that is related to a peak in the current density. This peak occurs at the region of the superconductor, where H_x is close to zero, then rotation predominates and J_y basically coincides with the parallel component ($J_\parallel \approx J_y$). Recall the similar phenomenon in figure 3 for the case of a normal metal. The difference here is that the peak of parallel current sits upon the step-like 'critical state' step profiles.

The second aspect to be recalled as regards the influence of Γ is compiled in figure 12. Here, we show the actual profiles of the transport current in the helical cable geometry, as one passes over the dissipation condition in a simulation that feeds a ramp of transport current along the sample. Noticeably, the transport profile in the isotropic situation goes from what is basically a step function below dissipation, towards a flat profile that fills the sample (and eventually goes beyond J_c) if more current is supplied. On the contrary, for the anisotropic case, the intermediate profiles display a peaked structure, and eventually become monotonous in the dissipation regime beyond the critical value. The current flows preferentially along the inner layers of the tape, once again advantaged by the parallel current condition. This effect may be explained through the predominance of self-field effects close to the periphery of the sample, in such a way that parallel current flow is enhanced towards the center.

5. Concluding remarks

The aim of this work was to provide a reliable expression of the material law to be used in wide range simulations of superconducting applications. More specifically:

(i) we have addressed the (frequently bypassed) question of modelling problems for which the current density is manifestly non-perpendicular to the magnetic field.
(ii) we have proposed to use a modified version of the popular power-law $\mathbf{E}(\mathbf{J})$ formula.

The main result of the paper is equation (10): $\mathbf{e}(\mathbf{j}) = \left(j^2 + \gamma\, j_\parallel^2\right)^{M-1} (\mathbf{j} + \gamma\, \mathbf{j}_\parallel)$ with $\mathbf{j}$ the dimensionless current density and $j_\parallel$ its projection onto the local magnetic field. We name it after 'elliptic-power-law' model. This expression incorporates the well reported fact that in a type-II

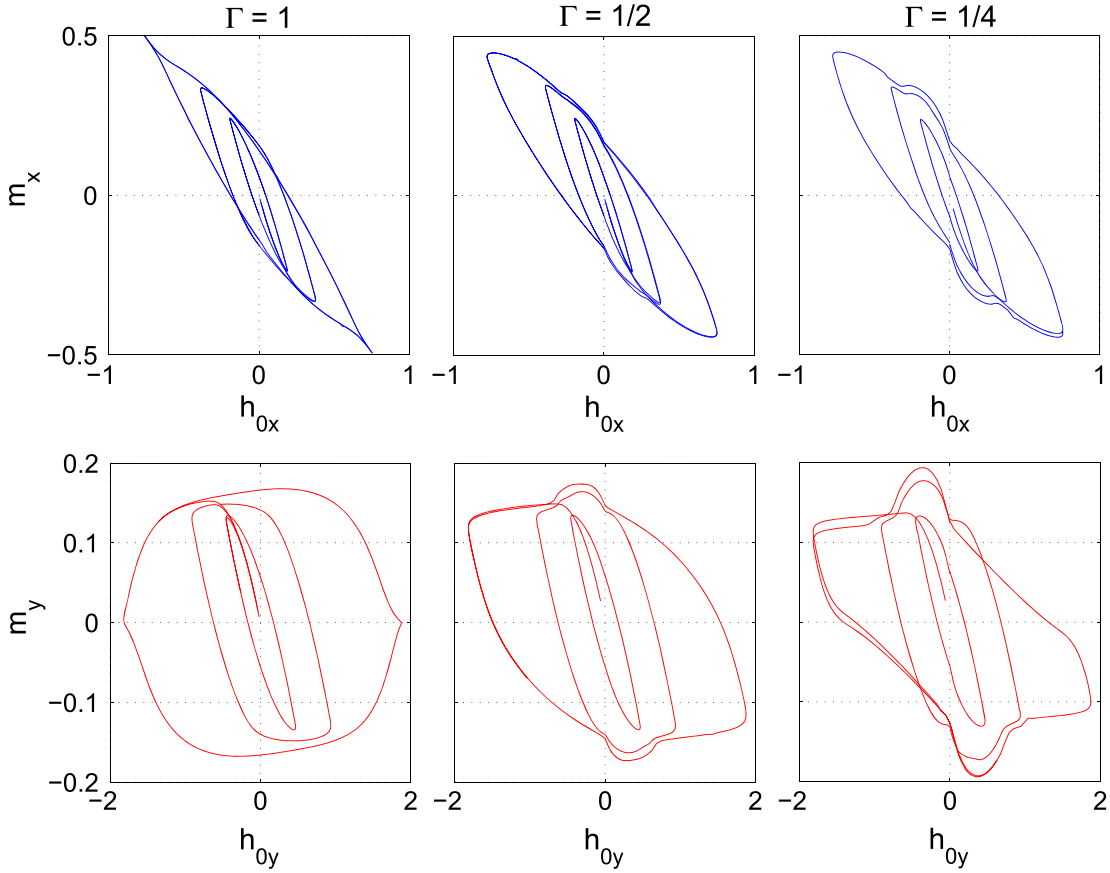

Figure 10. Magnetization loops related to the currents circulating along the outer superconducting layer for the system defined in figure 8. A cyclic process of the transport current along the system was assumed that produces a magnetic field (h_{0x}, h_{0y}) in the intermediate region. **H** is given in units of $J^*_{c\perp}d/2$, and the magnetic moment in units of $J^*_{c\perp}d^2/4$ with d the thickness of the slab. Here, we have used $\alpha_1 = \alpha_2 = 0$, $\beta_1 = \beta_2 = 67.5°$.

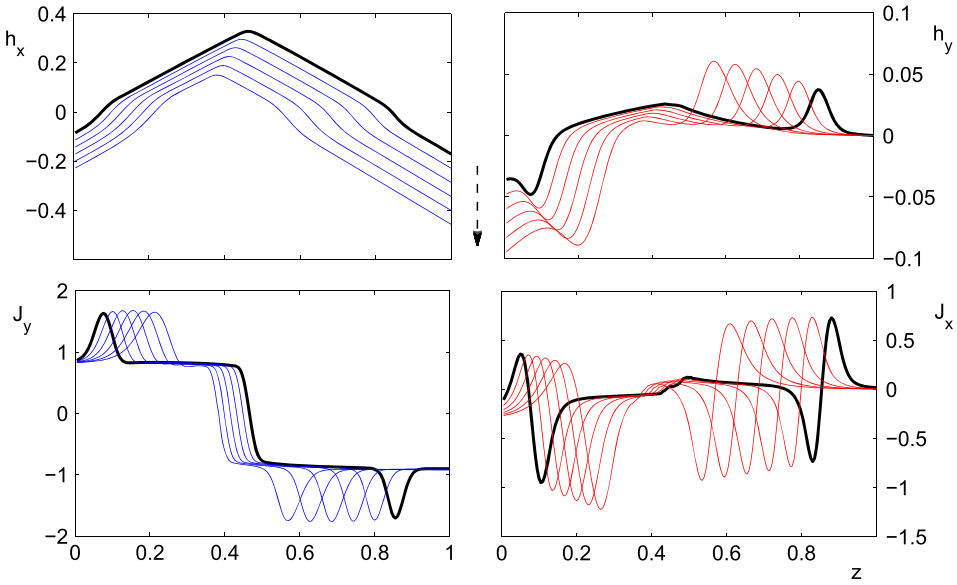

Figure 11. Profiles of the magnetic field and current density penetrating the superconductor in the configuration studied in figure 10, for the case $\Gamma = 1/2$. **H** is given in units of $J^*_{c\perp}d/2$, **J** in units of $J^*_{c\perp}$ and z normalized to the width d. $z = 0$ means the inner part of the slab. The arrow indicates the evolution of the boundary conditions.

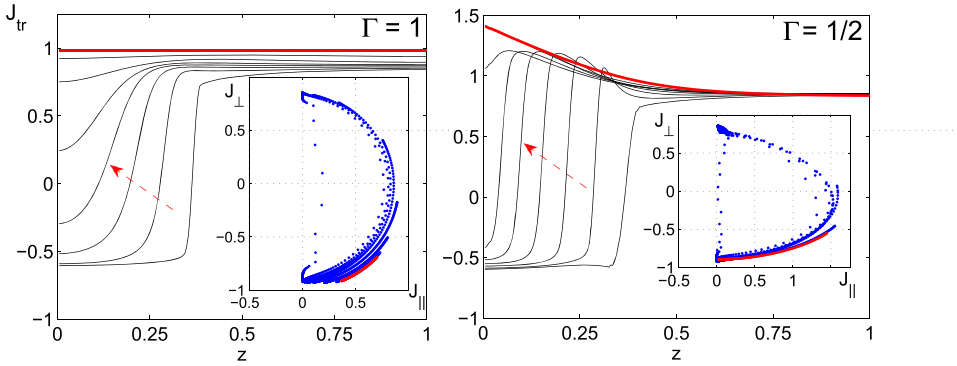

Figure 12. Simulation of the transport current penetration profiles across the thickness of the outer layer of the system in figure 8. In the simulation, a ramp of increasing transport current is fed through the layers of the double cable, in this case consisting of four layers at angles $\alpha_1 = 22.5$, $\alpha_2 = -22.5$ $\beta_1 = -22.5$ $\beta_2 = 22.5°$. A selection of current density profiles for increasing transport current is shown for the isotropic case $\Gamma = 1$ (left) and also for the anisotropic condition $\Gamma = 1/2$ (right). The insets display the map of points $J_{c\perp}(J_{c\parallel})$ corresponding to the data in the J_{tr} (z) curves.

superconductor with pinning, the equilibrium of flux lines is dependent on the angle between **J** and **B**. Thus, γ parametrizes the ratio between the maximum (critical) superconducting current densities $J^*_{c\parallel}$, $J^*_{c\perp}$ related to the extreme situations $\mathbf{J}\parallel\mathbf{B}$ and $\mathbf{J}\perp\mathbf{B}$. Equation (10) is ready to be incorporated in finite element codes, and is supported by experimental measurements [20] as well as by rather general theoretical arguments [16]. In fact, section 3 incorporates our proposal that the equation means nothing but assuming a common origin for the pinning interaction that prevents flux compression or rotation away from equilibrium.

With the background idea that the $\mathbf{E}(\mathbf{J})$ law encodes the physical behavior of the superconductor that has been driven away from equilibrium, we have addressed a couple of questions. First, related to the experimental procedures that allow to obtain the critical parameters $J^*_{c\parallel}$, $J^*_{c\perp}$ from non-equilibrium measurements:

(i) On the one side, we give an expression that quantifies the error in the 'eccentricity' ratio γ in terms of the voltage criterion used to obtain $\mathbf{J}_c(\theta)$, i.e.: the angular dependence of the critical current.
(ii) On the other side, we have quantified the relevance of the magnitude of the applied magnetic field and sample finite size effects in the $\mathbf{J}_c(\theta)$ measurements.

Finally, we also provide examples of the numeric application of our model on a practical system that involves a considerable amount of parallel current, i.e.: a stack of superconducting layers carrying current along crossed directions. By using a variational algorithm that is equivalent to the power-law elliptic model

(i) We have shown that increasing the value of the power M converges towards the critical state behavior, characterized by the geometric rule $\mathbf{J} \in \Omega_c$, with Ω_c the 'critical contour'. This condition means: whenever induced, current density takes the critical value. However, when M diminishes, the sample explores a band of values around the critical boundary, if driven away from equilibrium. This band gets narrower as M increases.
(ii) Some fingerprints of anisotropy (i.e.: $J^*_{c\parallel} \neq J^*_{c\perp}$) on the distribution of current density within the superconductor have been identified. For instance, if we assume the typical situation $J^*_{c\parallel} > J^*_{c\perp}$ an enhancement of the transport capacity occurs in the considered geometry. This means that a non-uniform current density profile with transport concentrated towards the inner part of the sample is obtained. Physically, as the angle between the current and the field is smaller in that region, and thus the critical current density is higher. On the other hand, anisotropy shows a characteristic feature (kink) in the predicted hysteresis loops.

In conclusion, we present support and applications of the elliptic-power-law model. In its mathematical form it is ready for application in massive finite element calculations for realistic systems such as helical structures or Roebel cables. Other relevant issues as the consideration of material anisotropies can be incorporated [27] through the dependence of the critical parameters $J^*_{c\parallel}$, $J^*_{c\perp}$ on the orientation of the local field relative to some material axis.

Acknowledgements

Funding of this research by Spanish MINECO and the European FEDER Program (Projects MAT2011-22719, ENE2011-29741 and MTM2012-33575) and by Gobierno de Aragón (Research group T12) is gratefully acknowledged.

References

[1] Rhyner J 1993 *Physica* C **212** 292
[2] Bean C P 1964 *Rev. Mod. Phys.* **36** 31
[3] Blatter G, Feigel'man M V, Geshkenbein V B, Larkin A I and Vinokur V M 1994 *Rev. Mod. Phys.* **66** 1125 and references therein

[4] Yamafuji K and Kiss T 1997 *Physica* C **290** 9
[5] Badía-Majós A and López C 2012 *Supercond. Sci. Technol.* **25** 104004
[6] Campbell A M and Evetts J E 1972 *Adv. Phys.* **21** 199 and references therein
[7] Walmsley D G 1971 *J. Phys. F: Met. Phys.* **2** 510
Walmsley D G and Timms W E 1977 *J. Phys. F: Met. Phys.* **7** 2373
[8] Cave J R and Evetts J E 1978 *Phil. Mag.* B **37** 111
[9] Matsushita T, Shimogawa A and Asano M 1998 *Physica* C **298** 115
[10] Clem J R 1980 *J. Low Temp. Phys.* **38** 353
Brandt E H 1980 *J. Low Temp. Phys.* **39** 41
[11] Voloshin I F *et al* 1991 *JEPT Lett.* **53** 115
[12] Fisher L M *et al* 1997 *Solid State Commun.* **103** 313
[13] LeBlanc M A R, Celebi S, Wang S X and Plechacek V 1993 *Phys. Rev. Lett.* **71** 3367
[14] Clem J R and Pérez-González A 1984 *Phys. Rev.* B **30** 5041
[15] Ruiz H S, López C and Badía A 2011 *Phys. Rev.* B **83** 014506
[16] Matsushita T 2014 *Flux Pinning in Superconductors* (Berlin: Springer)
Matsushita T 2012 *Japan. J. Appl. Phys.* **51** 010111
[17] Badía-Majós A, López C and Ruiz H S 2009 *Phys. Rev.* B **80** 144509
[18] Brandt E H, Clem J R and Walmsley D G 1979 *J. Low Temp. Phys.* **37** 43
[19] Orlando T P and Delin K A 1991 *Foundations of Applied Superconductivity* (Englewood Cliffs, NJ: Prentice-Hall)
[20] Clem J R, Weigand M, Durrell J H and Campbell A M 2011 *Supercond. Sci. Technol.* **24** 062002
[21] Campbell A M 2011 *Supercond. Sci. Technol.* **24** 091001
[22] Pitel J and Kováč P 2011 *Physica* C **471** 1680
[23] Nii M, Amemiya N and Nakamura T 2012 *Supercond. Sci. Technol.* **25** 095011
Zermeno V M, Grilli F and Sirois F 2013 *Supercond. Sci. Technol.* **26** 052001
[24] Clem J R and Malozemoff A P 2010 *Supercond. Sci. Technol.* **23** 034014
[25] Badía-Majós A, Cariñena J F and López C 2009 *J. Phys. A: Math. Theor.* **39** 14699
[26] Walmsley D G 1972 *J. Phys. F: Met. Phys.* **2** 510
[27] Amigo M L, Ale Crivillero V, Franco D G, Badía-Majós A, Guimpel J and Nieva G 2014 *J. Phys.: Conf. Ser.* **507** 012001